RSC Advances

ROYAL SOCIETY OF CHEMISTRY

www.rsc.org/advances

RSC Advances

COMMUNICATION

Rational design of Sn-based multicomponent anodes for high performance lithium-ion batteries: SnO_2@TiO_2@reduced graphene oxide nanotubes

Received 00th January 20xx,
Accepted 00th January 20xx

DOI: 10.1039/x0xx00000x

www.rsc.org/

Jun Young Cheong, † Chanhoon Kim, † Ji Soo Jang, and Il-Doo Kim*

Ultra thin TiO_2 layer (2 nm)-coated SnO_2 nanotubes (NTs) wrapped by reduced graphene oxide (rGO) sheets (SnO_2@TiO_2@rGO) were synthesized as high capacity anode materials for lithium-ion batteris. The rationally designed anodes exhibited superior rate capability while maintaining high discharge capacity of over 840 mAh g^{-1} at a current density of 500 mA g^{-1} after 50 cycles.

As both the next-generation renewable energy sources and highly efficient energy storage devices, lithium-ion batteries (LIBs) have been commercialized to some extents in electric vehicles, cell phones, and other storage devices.[1-4] Nevertheless, conventional LIBs with graphite anodes have limitations in large theoretical capacity (372 mAh g^{-1}), desired for large-scale electric grids and energy storage system.[5-8] As for the LIBs with higher energy density, metal oxides have been suggested as the promising anode candidates, due to their inexpensive costs, high theoretical capacity, and safety characteristics.[9–11] Among them, tin (IV) oxide (SnO_2) is one of the promising anode materials for LIBs, due to its higher theoretical capacity (782 mAh g^{-1}), enhanced battery safety, and good chemical stability with electrolytes.[12-16]

However, several drawbacks exist for SnO_2 anodes in LIBs including: i) severe volume expansion (>300%) during cycling which leads to poor cycling retention; ii) formation of unstable solid electrolyte interphase (SEI) layer; and iii) low electrical conductivity.[17-18] In order to resolve these issues, numerous attempts have been made.[19-22] For instance, different researches on Sn-C composite materials have been initially devised and suggested, and they were aimed at utilizing carbon to increase the low electrical conductivity of SnO_2 and Sn.[23–25] With this approach, however, increasing loading amount of carbon results in decreasing loading amount of either Sn or SnO_2, which lead to lower capacity. Another approach has been made to utilize titanium dioxide (TiO_2) with tin oxide to make a composite anode material. Combining with TiO_2, it forms stable solid-electrolyte interphase (SEI) layer, thereby contributing to more stable nanostructure that maintains structural integrity during lithiation/de-lithiation, with better cycle retention for longer cycles.[26,27] Different research strategies have been suggested such as TiO_2 nanotubes@SnO_2 nanoflakes, TiO_2/SnO_2/carbon hybrid nanofiber using thermal pyrolysis, SnO_2@TiO_2 double-shell nanotubes, and SnO_2@TiO_2 nanowires through atomic layer deposition (ALD).[27-30] Nevertheless, the limitation for these approaches is that general synthetic methods were rather complicated series of steps and not applicable for large-scale synthesis.

In this research, we have successfully synthesized ultra thin TiO_2 layer (2 nm)-coated SnO_2 NTs (hereafter, SnO_2@TiO_2 NTs) via electrospinning method, seqsequent calcination process, and sol-gel process. With uniform TiO_2 coating layer on SnO_2 NTs, it forms a stable SEI layer, which then enhances cycle retention and structural integrity. In addition, upon reduced graphene oxide (rGO) wrapping, rGO-wrapped SnO_2@TiO_2 NTs (SnO_2@TiO_2@rGO NTs) were formed, where the electrical conductivity was singnificantly increased. With facile and simple synthetic sol-gel methods distinct from the previous works on SnO_2/TiO_2, it forms stable SEI layer, resulting in better cycle retention. Subsequently, rate capability is also improved by rGO wrapping on SnO_2@TiO_2 NTs.

The synthesis of SnO_2@TiO_2@rGO NTs was prepared via electrospinning process, calcination treatment, sol-gel process,

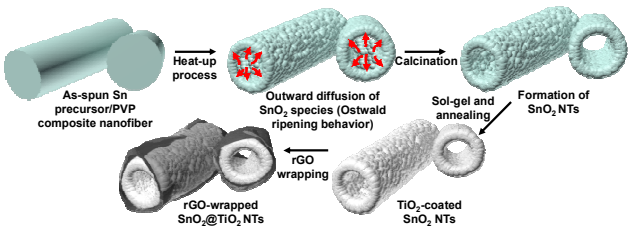

Fig. 1 Schematic illustration on the formation process of SnO_2, SnO_2@TiO_2, and SnO_2@TiO_2@rGO NTs.

Department of Materials Science and Engineering, Korea Advanced Institute of Science and Technology, 291 Daehak-ro, Yuseong-gu, Daejeon, 305-701, Republic of Korea. E-mail: idkim@kaist.ac.kr
† These authors contributed equally to this work.
Electronic Supplementary Information (ESI) available. See DOI: 10.1039/x0xx00000x

and solution-based reduced graphene oxide (rGO)-wrapping process, as illustrated in Fig. 1. Using single-nozzle electrospinning process, Sn precursor/poly(vinylpyrrolidone) (PVP) composite nanofibers (NFs) were fabricated. Upon calcination process at 600 °C for 1 h and 700 °C for 1 h, SnO_2 NTs were formed by Kirkendall effect in the following steps[31]: i) as temperature increased, PVP was decomposed and tin (Sn) precursor on the outer surface of the fibers was oxidized and became SnO_2; ii) Sn precursor at the core is also subsequently oxidized and with the Ostwald ripening allows the oxidized Sn at the core to move to the outer SnO_2 with larger grain sizes, in addition to the fact that CO_2 gas and H_2O gas from decomposition of PVP also moves Sn precursor at the core to the outer side; iii) at the same time, inward flow of vacancies moved to the core at the place where Sn precursor moved outward; iv) finally, upon subsequent temperature increase, SnO_2 underwent nanograin formation, growth, and reorganization, as shown in the previous literature.[32]

Surface morphology of as-spun Sn precursor/PVP NFs, SnO_2, SnO_2@TiO_2, and SnO_2@TiO_2@rGO NTs is shown in Fig. 2. The scanning electron microscopy (SEM) image of Sn precursor/PVP composite NFs with diameter ranged between 300 and 500 nm, is shown in Fig. 2a. The Sn precursor/PVP composite NFs were converted to SnO_2 NTs consisting of SnO_2 nanograins that have mean grain sizes of 30.6 nm calculated from Scherrer's equation (1) for the (110) peak in Fig. S1 after calcination (Fig. 2b):

$$\tau = \frac{K\lambda}{\beta \cos\theta} \quad (1)$$

where τ is crystallite size of SnO_2, K is a dimensionless shape factor, λ is the X-ray wavelength, β is the line broadening at half the maximum intensity, and θ is the Bragg angle. Subsequently, TiO_2 layer was adopted on the surface of the SnO_2 NTs via sol-gel process. Fig. 2c shows the SEM image of SnO_2@TiO_2 NTs, with smoother surface morphology of shells than that of SnO_2 NTs. The hollow structure of as-synthesized samples is well maintained during sol-gel process of TiO_2, with surface area of 7.76 m^2 g^{-1}, as shown in Fig. S2.

To clearly analyze the surface morphology and crystal structure, we carried out transmission electron microscopy (TEM) analysis. Fig. 2d shows the overall morphology of SnO_2@TiO_2 NTs with uniform thickness across different areas. It can be shown from Fig. 2e that about 2 nm (solid yellow line) of TiO_2 layer was uniformly present on the surface of SnO_2. To illustrate the spatial distribution of SnO_2 and TiO_2, transmission electron microscopy energy-dispersive X-ray spectroscopy (TEM-EDS) elemental mapping was performed on as-synthesized SnO_2@TiO_2 NTs (Fig. 2f). According to the elemental mapping images of SnO_2@TiO_2 NTs, TiO_2 layers were conformally coated on the surface of SnO_2 nanograins. In the selected area electron diffraction (SAED) pattern of SnO_2@TiO_2 NTs (Fig. 2g), however, crystal structure of TiO_2 was not clearly shown, as it can be speculated that the concentration of TiO_2 was too minimal to have enough intensity to have a clear diffraction pattern, as shown from

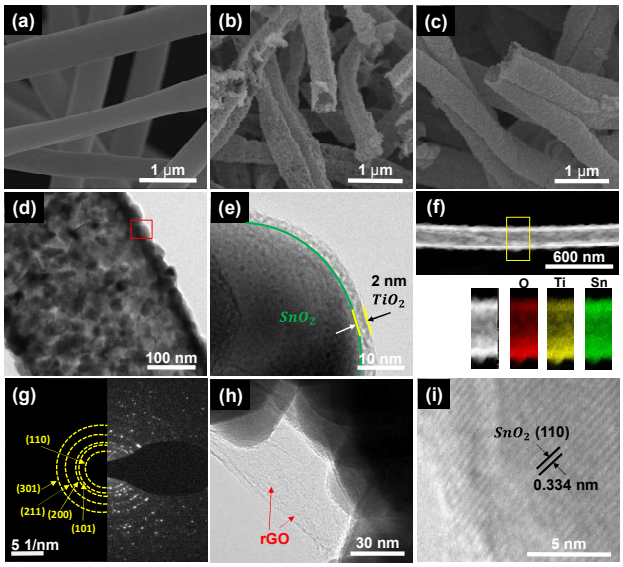

Fig. 2 SEM images of (a) electrospun Sn precursor/PVP NFs, (b) SnO_2 NTs, and (c) SnO_2@TiO_2 NTs. (d) TEM images of (d) SnO_2@TiO_2 NTs. (e) Magnified TEM image of the the red frame in (d), which indicates TiO_2-coated outer layer of SnO_2@TiO_2 NTs. (f) TEM elemental mapping images of SnO_2@TiO_2 NTs according to each element (O, Ti, and Sn). (g) SAED pattern of SnO_2@TiO_2 NTs. TEM images of (i) SnO_2@TiO_2@rGO NTs showing the wrapped rGO layers and (h) SnO_2@TiO_2@rGO NTs having lattice spacing of SnO_2.

previous literature.[30]

To clearly confirm the crystal structure of TiO_2, another sample with five times higher concentration of Ti precursor (denoted as SnO_2@ TiO_2 (X5)) was prepared. Fig. S3a shows the TEM images of SnO_2@TiO_2 (X5) NT and Fig. S3b shows its magnified image of red box. The marked interplanar d spacing of 0.352 nm corresponds to the (101) lattice plane of anatase TiO_2. The SAED pattern of SnO_2@TiO_2 (X5) sample indicates the polycrystalline nature of the as-synthesized sample and the diffraction rings can be readily assigned to the SnO_2 and dominant peaks of anatase TiO_2 such as (101), (004), and (204), which were shown in Fig. S3c. This anatase structure was also confirmed through X-ray diffraction (XRD) pattern of SnO_2@TiO_2 (X5) (Fig. S3d), where anatase peaks were clearly apparent in the lattice planes of (101) and (200) at 25.3° and 48.0°.[33–34]

Upon rGO wrapping, rGO layers were coated on TiO_2 layer and TEM image of SnO_2@TiO_2@rGO is shown in Fig. 2h, where the thin layers of rGO are shown on the outer side of SnO_2@TiO_2 NTs. Lattice spacing of SnO_2 in SnO_2@TiO_2@rGO NTs was shown in Fig. 2i, which was also in agreement with the XRD pattern of SnO_2 NTs.[35-37] Based on thermogravimetric analysis (TGA) in air of the SnO_2@TiO_2@rGO NTs, it was calculated that the rGO content was ca. 3.10 wt% in the as-synthesized sample (Fig. 3a).[38–39]

Fig. 3b shows the Raman spectrum of SnO_2@TiO_2@rGO NTs. Two peaks at 1343 cm^{-1} and 1599 cm^{-1}, which corresponded to the D and G band of characteristic carbon peaks, were found

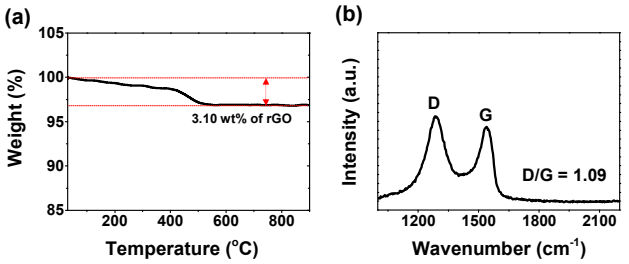

Fig. 3 (a) TGA curve and (b) Raman spectra of SnO_2@TiO_2@rGO.

and the dimensional ratio of the D band to the G band for the sample was estimated to be 1.09, which indicates the formation of amorphous carbon which are in good agreement with Raman peaks of rGO in similar designs of materials.[40–42]

Surface chemical states of SnO_2@TiO_2 and SnO_2@TiO_2@rGO NTs were also analyzed using x-ray photoelectron spectroscopy (XPS). XPS spectra of Sn and Ti in SnO_2@TiO_2 NTs are presented in Fig. 4a and Fig. 4b, respectively. Sn^{4+} $3d_{3/2}$ and $3d_{5/2}$ have binding energy peaks at 495.0 and 486.6 eV, which are similar to the previously reported values.[28] Ti^{4+} $2p_{1/2}$ and $2p_{3/2}$ have binding energy peaks at 464.5 and 458.8 eV, which are also similar to the previously reported values.[28,43] XPS spectra of Sn and Ti in SnO_2@TiO_2@rGO NTs are presented in Fig. 4c and Fig. 4d, respectively. Sn^{4+} $3d_{3/2}$ and $3d_{5/2}$ have binding energy peaks at 495.5 and 487.1 eV, which are similar to the previously reported values.[28] Ti^{4+} $2p_{1/2}$ and $2p_{3/2}$ have binding energy peaks at 465.0 and 459.3 eV, which are also similar to the previously reported values.[28,44] In summary, XPS spectra for SnO_2@TiO_2 and SnO_2@TiO_2@rGO NTs confirmed that SnO_2 and TiO_2 are present.

A series of electrochemical characterizations were carried out to investigate the electrochemical properties of the SnO_2, SnO_2@TiO_2, and SnO_2@TiO_2@rGO NTs based electrodes using 2032-type coin cells. The detailed cell fabrication procedure was described in supporting information. Fig. S4 shows cyclic voltammogram (CV) curves of the first, second and third cycles of SnO_2@TiO_2 NTs within the range of 0.01–3.0 V vs. Li/Li^+ at a scan rate of 0.1 mVs^{-1}. Typically, it is widely known that electrochemical reaction of SnO_2 involves two steps (reduction of SnO_2 and alloying and de-alloying of Sn) and Li insertion/de-insertion reaction of TiO_2 is an intercalation reaction, as shown in the reactions below:[30,45,46]

$SnO_2 + 4Li^+ + 4e^- \rightarrow Sn + 2Li_2O$ (reduction of SnO_2)

$xLi^+ + xe^- + Sn \leftrightarrow Li_xSn$ ($0 \leq x \leq 4.4$) (alloying/de-alloying of Sn)

$TiO_2 + xLi^+ + xe^- \leftrightarrow Li_xTiO_2$ (Li insertion/deinsertion of TiO_2)

In the first cycle, a cathodic peak of 0.75 V was observed in the discharge process, which can be ascribed to the reduction of SnO_2 to Sn and the formation of Li_2O as well as formation of SEI layer, in accordance with the previous literature.[45,52] This process usually occurs at a voltage higher than 0.6 V and is generally known to be irreversible.[47-50] Second cathode peak of

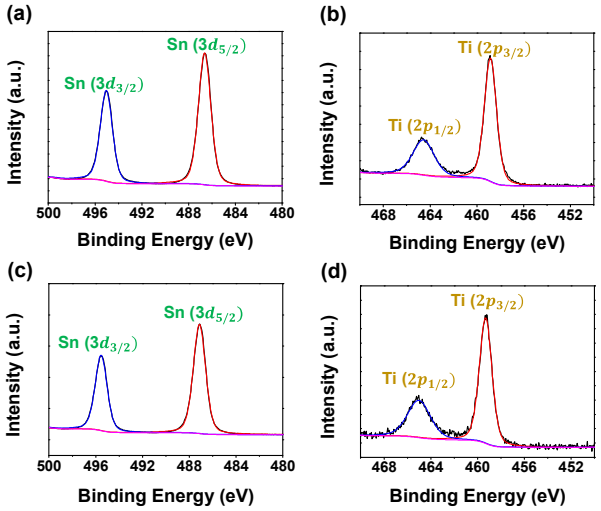

Fig. 4 XPS spectrum of (a) Sn, (b) Ti in SnO_2@TiO_2 NTs and (c) Sn, (d) Ti in SnO_2@TiO_2@rGO NTs.

of 0.3 V was observed in the discharge process, which accounts for the alloying of Sn to Li_xSn. Alloying process occurs at a lower voltage and is known to be reversible.[51] With the formation of Li_2O and SEI layer in the 1st cycle, the general reaction becomes reversible after the 1st cycle, where CV curves do not vary significantly from the 2nd to 3rd cycle in the discharge process, indicating that the reaction has proceeded with the alloying reaction. At the same time, small peaks at 1.0 V and 1.5 V are mainly attributed to the reaction between Li and TiO_2, which is broadly coated on the surface of SnO_2.[53] This concurs with the previous study that initial CV curve of TiO_2 starts with -0.4 mA at 1.0 V, and shows one broad peak at 1.5 V.[52] From the 2nd to 3rd cycle in the charge process, two peaks at 0.6 V and 1.3 V are related to the de-alloying of Li_xSn and oxidation of Sn to SnO_2 and it is suggested that small peak at 1.75 V is mainly due to the single-phase Li-insertion/de-insertion reaction in TiO_2.[52] Presence of smooth, small CV peaks for TiO_2 is in agreement with the previous observation that nano-sized systems result in smaller, broader peaks rather than sharp peaks.[54]

To examine the initial irreversible capacity loss as a result of conversion reaction (reduction of SnO_2), the first charge and discharge profiles of SnO_2, SnO_2@TiO_2, and SnO_2@TiO_2@rGO NTs were analyzed in the voltage range of 0.005–3.0 V at a current density of 50 mA g^{-1}, as shown in Fig. 5a. SnO_2, SnO_2@TiO_2, and SnO_2@TiO_2@rGO NTs have initial discharge capacity of 1429.2 mAh g^{-1}, 1312.5 mAh g^{-1}, and 1531.7 mAh g^{-1} and initial charge capacity of 944.3 mAh g^{-1}, 873.8 mAh g^{-1}, and 1029.2 mAh g^{-1}, which correspond to the initial coulombic efficiency of 66.1%, 66.6%, and 67.2% for SnO_2, SnO_2@TiO_2, and SnO_2@TiO_2@rGO NTs, with similar efficiencies. The capacity values are higher than the theoretical capacity of SnO_2 (782 mAh g^{-1}) and theoretical capacity of SnO_2@TiO_2@rGO ($C_{SnO2@TiO2@rGO} = C_{SnO2*\%\ SnO2\ mass} + C_{rGO*\%\ rGO\ mass}$ = (782) X (0.969) + (372) X (0.031) = 769.3 mAh g^{-1}), which is attributed to the synergistic effects of different components.

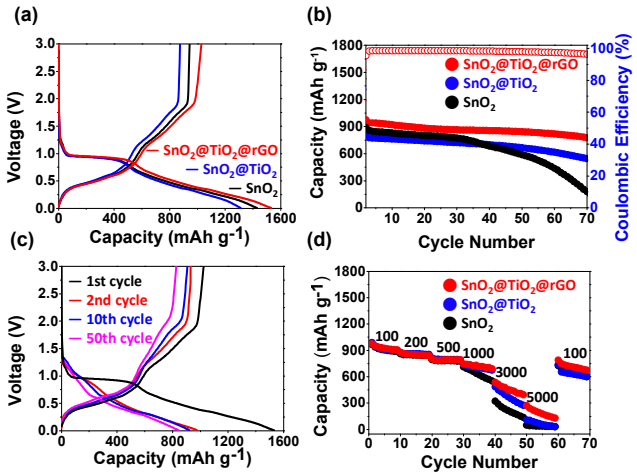

Fig. 5 Electrochemical performances of SnO_2@TiO_2@rGO, SnO_2@TiO_2, and SnO_2 NTs. (a) Galvanostatic first cycle discharge/charge curves at a current density of 50 mA g^{-1} between 0.005 V and 3.0 V. (b) Cycle performance of various samples at a current density of 500 mA g^{-1} between 0.01 V and 3.0 V. (c) Variation in the discharge/charge profiles of SnO_2@TiO_2@rGO during cycling at a current density of 500 mA g^{-1}. (d) Rate capabilities of various samples. The same discharge/charge rate was used from 100 – 5000 mA g^{-1} between 0.01 V – 3.0 V.

To understand the effect of coated TiO_2 and wrapped rGO layer on cycle retention, SnO_2, SnO_2@TiO_2, and SnO_2@TiO_2@rGO NTs were cycled at a current density of 500 mA g^{-1} for 70 cycles, as presented in Fig. 5b. Electrochemical properties of SnO_2 NTs made under different calcination temperatures were tested, and it was shown that the condition for calcination described above was the optimal condition, as shown in the Fig. S5. Comparing the cycle retention of SnO_2 NTs, SnO_2@TiO_2, and SnO_2@TiO_2@rGO from the 2nd cycle to 70th cycle, it is evident that SnO_2@TiO_2@rGO exhibits better cycle retention (79.7%) compared with that of pristine SnO_2 (20.3%) and SnO_2@TiO_2 (67.1%) NTs. Coulombic efficiency of SnO_2@TiO_2@rGO NTs maintains a stable state up to 70 cycles, which suggests that enhanced capacity retention is mainly attributed to the hybrid structure that forms stable SEI layer by coating TiO_2 layer and increases electrical conductivity by wrapping rGO layers. In addition, the charge and discharge profile of SnO_2@TiO_2@rGO and SnO_2@TiO_2 NTs at a current density of 500 mA g^{-1} are shown in Fig. 5c and Fig. S6.

In order to demonstrate that thin TiO_2 layer on the surface of SnO_2 helps to form more thin and stable SEI layer, we conducted ex-situ SEM analysis of electrodes after 50 cycles at 500 mAg^{-1}. The thinner and smoother SEI layer was formed on the surface of SnO_2@TiO_2 after 50 cycles at 500 mAg^{-1} than that of SnO_2 in the SEM images (Fig. S7a and b). Furthermore, we observed that thinner and smoother SEI layer was formed on the surface of SnO_2@TiO_2@rGO than both SnO_2 and SnO_2@TiO_2 (Fig. S7c). Owing to the formation of thin and stable SEI layer on the surface, SnO_2@TiO_2@rGO shows much improved cycle retention and reversible capacity.

The initial irreversible capacity of both SnO_2@TiO_2 and SnO_2@TiO_2@rGO NTs comes from the formation of Li_2O, an amorphous matrix, and SEI layer.[47,48] After the 2nd cycle, both the discharge and charge capacity of SnO_2@TiO_2 NTs decreased from 812.7 mAh g^{-1} to 655.3 mAh g^{-1} and from 769.4 mAh g^{-1} to 642.6 mAh g^{-1}, showing capacity retention less than 85%. On the other hand, after the 2nd cycle, both the discharge and charge capacity of SnO_2@TiO_2@rGO NTs only slightly decreased from 974.8 mAh g^{-1} to 843.3 mAh g^{-1} and from 930.8 mAh g^{-1} to 825.8 mAh g^{-1}, maintaining capacity above 800 mAh g^{-1} with better capacity retention even after 50 cycles.

To understand the effect of rGO layer in enhancement of electrical conductivity, we evaluate the rate capabilities of SnO_2, SnO_2@TiO_2, and SnO_2@TiO_2@rGO NTs at various current densities (Fig. 5d). SnO_2@TiO_2@rGO NTs exhibited better rate capabilities compared with both SnO_2@TiO_2 and SnO_2 NTs, especially at higher current densities, which can be suggested from the improved electrical conductivity with rGO-wrapping process that can be demonstrated by impedance tests. Fig. S8 shows the Nyquist plot of each sample after 50th cycle. Semicircles in different frequency regions are ascribed to different factors: semicircle in high frequency region is attributed to the contact resistance by SEI layer formation; semicircle in middle frequency region is attributed to the charge transfer resistance; the straight line in low frequency region describes the mass transfer of lithium ions.[55,56] After the 50th cycle, it is clearly shown that the charge-transfer resistance (R_{ct}) of SnO_2@TiO_2@rGO is much smaller compared with those of SnO_2@TiO_2 and SnO_2 NTs. Such trends of semicircle areas in Nyquist plots can be suggested that SnO_2@TiO_2@rGO, upon rGO-wrapping, greatly improved the electrical conductivity of SnO_2@TiO_2, maintained even after 50 cycles.[57,58]

Conclusions

In this work, we successfully synthesized a new hybrid structure of SnO_2@TiO_2@rGO NTs. The anode electrode with SnO_2@TiO_2@rGO NTs exhibited excellent cycle retention and good rate capabilities compared with SnO_2@TiO_2 and SnO_2 NTs. Such outstanding features are attributed to the following reasons: i) With electrospinning and subsequent calcination, SnO_2 NTs were formed, which maintain structural integrity and allow shorter Li-ion diffusion path; ii) Sol-gel process of TiO_2 on SnO_2 NTs allows TiO_2 coated layer to act as a surface protection layer which provides stable SEI layer; iii) Upon rGO-wrapping, electrical conductivity was improved, which facilitates charge transport to the active material, leading to superior rate capability at higher c-rates. Our suggested strategy that incorporates both thin TiO_2 overlayer and rGO sheets can be applied to other anode materials, such as Si, to both enhance the cycle retention and rate capability.

Acknowledgements

This work was supported by the Korea CCS R&D Center (KCRC) grant funded by the Korea government (Ministry of Science, ICT & Future Planning) (No. NRF-2014M1A8A1049303) and End-Run grant from KAIST funded by the Korea government in 2015 (Ministry of Science ICT & Future Planning) (N01150615).

Notes and references

1 J. M. Tarascon, M. Armand, *Nature*, 2001, **414**, 359.
2 G.-A. Nazri, G. Pistoia, *Lithium Batteries: Science and Technology*, Kluwer Academic/Plenum, Boston, 2004.
3 V. Etacheri, R. Marom, R. Elazari, G. Salitra, D. Aurbach, *Energy Environ. Sci.*, 2011**, 4**, 3243.
4 B. Scrosati, J. Garche, *J. Power Sources*, 2010, **195**, 2419.
5 J. Luo, X. Xia, Y. Luo, C. Guan, J. Liu, X. Qi, C. F. Ng, H. Zhang, H. J. Fan, *Adv. Energy Mater.*, 2013, **3**, 737.
6 C. Zhu, X. Xia, J. Liu, Z. Fan, D. Chao, H. Zhang, H. J. Fan, *Nano Energy*, 2014, **4**, 105.
7 P. G. Bruce, S. A. Freunberger, L. J. Hardwick, J.-M. Tarascon, *Nature Materials*, 2012, **11**, 19.
8 M. Ge, J. Rong, X. Feng, C. Zhou, *Nano Letters*, 2012, **12***,* 2318.
9 W. Wei, Z. Wang, Z. Liu, Y. Liu, L. He, D. Chen, A. Umar, L. Guo, J. Li, *J. Power Sources*, 2013**, 238**, 376.
10 X. Wang, X. Li, X. Sun, F. Li, Q. Liu, Q. Wang, D. He, *J. Mater. Chem.*, 2011, **21**, 3571.
11 C. Jiang, E. Hosono, H. Zhou, *Nano Today*, 2006, **1**, 28.
12 L. Li, X. Yin, S. Liu, Y. Wang, L. Chen, T. Wang, *Electrochemistry Communications*, 2010, **12**, 1383-1386.
13 M.-S. Park, G.-X. Wang, Y.-M. Kang, D. Wexler, S.-X. Dou, H.-K. Liu, *Angew. Chem., Int. Ed.* 2007, **46**, 750.
14 B. Scrosati, *Nature,* 1995, **373***,* 557.
15 J. S. Chen, L. A. Archer, X. W. Lou, *J. Mater. Chem.*, 2011, **21**, 9912.
16 J. Lei, W. Li, X. Li, E. J. Cairns, *J. Mater. Chem.*, 2012, **22**, 22022.
17 B. Wang, B. Luo, X. Li, L. Zhi, *Mater. Today*, 2012, **15**, 544-552.
18 Y. D. Ko, J. G. Kang, J. G. Park, S. Lee, D. W. Kim, *Nanotechnology.*, 2009, **20**, 455701.
19 J. Zhu, G. Zhang, X. Yu, Q. Li, B. Lu, Z. Xu, *Nano Energy*, 2014, **3**, 80-87.
20 V. Aravindan, J. Sundaramurthy, E. N. Kumar, P. S. Kumar, W. C. Ling, R. V. Hagen, S. Mathur, S. Ramakrishna, S. Madhavi, *Electrochimica Acta*, 2014, **121**, 109-115.
21 X. M. Yin, C. C. Li, M. Zhang, Q. Y. Hao, S. Liu, L. B. Chen, T. H. Wang, *J. Phys. Chem. C.*, 2010, **114**, 8084-8088.
22 S.-M. Paek, E. Yoo, I. Honma, *Nano Lett.,* 2009, **9**, 72-75.
23 G. Derrien, J. Hassoun, S. Panero, B. Scrosati, *Advanced Materials*, 2007, **19**, 2336-2340.
24 Y. Xu, Q. Liu, Y. Zhu, Y. Liu, A. Langrock, M. R. Zachariah, C. Wang, *Nano Lett.*, 2013, **13**, 470-474.
25 A. Jahel, C. M. Ghimbeu, L. Monconduit, C. V.-Guterl, *Adv. Energy Mater.*, 2014, **4**, 1400025.
26 X. Wu, S. Zhang, L. Wang, Z. Du, H. Fang, Y. Ling, Z. Huang, *J. Mater. Chem.*, 2012, **22**, 11151-11158.
27 J.-H. Jeun, K.-Y. Park, D.-H. Kim, W.-S. Kim, H.-C. Kim, B.-S. Lee, H. Kim, W.-R. Yu, K. Kang, S.-H. Hong, *Nanoscale*, 2013, **5**, 8480.
28 C. Zhu, X. Xia, J. Liu, Z. Fan, D. Chao, H. Zhang, H. J. Fan, *Nano Energy*, 2014, **4**, 105-112.
29 Z. Yang, Q. Meng, Z. Guo, X. Yu, T. Guo, R. Zeng, *J. Mater. Chem.*, 2013, **1**, 10395.
30 C. Guan, X. Wang, Q. Zhang, Z. Fan, H. Zhang, H. J. Fan, *Nano Letters*, 2014, **14**, 4852-4858.
31 A. E. Mel, R. Nakamura, C. Bittencourt, *Beilstein J. Nanotechnol.* 2015, **6**, 1348-1361.
32 X. Xia, X. J. Dong, Q. F. Wei, Y. B. Cai, K. Y. Lu, *eXPRESS Polymer Letters*, 2012, **6**, 169-176.
33 R. Liu, D. Li, D. Tian, G. Xia, C. Wang, N. Xiao, N. Li, N. H. Mack, Q. Li, G. Wu, *J. Power Sources*, 2014, **251**, 281.
34 H. Kose, A. O. Aydin, H. Akbulut, *International Journal of Hydrogen Energy*, 2014, **39**, 21440.
35 Q. Fan, B. McQuillin, A. K. Ray, M. L. Turner, A. B. Seddon, *J. Phys. D: App. Phys.*, 2000, **33**, 2683-2686.
36 G. Q. Liu, Z. G. Jin, X. X. Liu, T. Wang, Z. F. Liu, *J. Sol-Gel Sci Techn.*, 2007, **41**, 49-55.
37 H. Wang, M. Wang, B. Li, X. Yang, K. Safarova, R. Zboril, A. L. Rogach, M. K. H. Leung, *CrystEngComm.*, 2014, **16**, 7531.
38 J. Yin, H. Shi, P. Wu, Q. Zhu, H. Wang Y. Tang, Y. Zhou, T. Lu, *New J. Chem*, 2014, **38**, 4037.
39 V. Chabot, K. Feng, H. W. Park, F. M. Hassan, A. R. Elsayed, A. Yu, X. Xiao, Z. Chen, *Electrochimica Acta*, 2014, **130**, 128.
40 C. Zheng, J. Wang, Z. Chen, H. Liu, *J. Phys. Chem. C.*, 2014, **115**, 25115-25120.
41 L. Shen, X. Zhang, H. Li, C. Yuan, G. Cao, *J. Phys. Chem. Lett.*, 2011, **2**, 3096-3101.
42 G. Xia, N. Li, D. Li, R. Liu, C. Wang, Q. Li, X. Lu, J. S. Spendelov, J. Zhang, G. Wu, *ACS Appl. Mater. Interphases*, 2013, **5**, 8607-8614.
43 G. Hopfengartner, D. Borgmann, I. Rademacher, G. Wedler, E. Hums, G. W. Spitznagel, *Journal of Electron Spectroscopy and Related Phenomna*, 1993, **63**, 91-116.
44 Y. Okazaki, T. Tateishi, Y. Ito, *Materials Transactions, JIM.*, 1997, **38**, 78-84.
45 W. Ren, C. Wang, L. Lu, D. Li, C. Cheng, J. Liu, *J. Mater. Chem. A.*, 2013, **1**, 13435.
46 Z. Wang, X. W. Lou, *Adv. Mater.*, 2012, **24**, 4124-4129.
47 I. A. Courtney, J. R. Dahn, *J. Electrochem. Soc.*, 1997, **144**, 2050-2052.
48 H. Kim, S.-W. Kim, Y.-U. Park, H. Gwon, D.-H. Seo, Y. Kim, K. Kang, *Nano Res.*, 2010, **3**, 813-821.
49 M. Winter, J. O. Besenhard, *Electrochimica Acta.*, 1999, **45**, 42.
50 P. A. Connor, J. T. S. Irvine, *J. Power Sources*, 2001, **97-98***,* 223.
51 C. J. Wen, R. A. Huggins, *J. Electrochem. Soc.*, 1981, **128**, 1186.
52 G. Zhou, D.-W. Wang, L. Li, N. Li, F. Li, H.-M. Cheng, *Nanoscale*, 2013, **5**, 1579.
53 V. Aravindan, N. Shubha, Y. L. Cheah, R. Prasanth, W. Chuiling, R. R. Prabhakar, S. Madhavi, *J. Mater. Chem. A.*, 2013, **1**, 311.
54 Y. Ren, Z. Liu, F. Pourpoint, A. R. Armstrong, C. P. Grey, P. G. Bruce, *Angew. Chem. Int. Ed.*, 2012, **51**, 2165.
55 C. Kim, J. Y. Jang, N. S. Choi, S. Park, *RSC Adv.*, 2014, **4**, 3070-3074.
56 S. H. Choi, Y. C. Kang, *ChemSusChem.*, 2013, **6**, 2111-2116.
57 J. Shin, K. Park, W.-H. Ryu, J.-W. Jung, I. D. Kim, *Nanoscale*, 2014, ***6***, 12718.
58 J.-H. Choi, W.-H. Ryu, K. Park, J.-D. Jo, S.-M. Jo, D.-S. Lim, I.-D. Kim, *Scientific Reports*, 2014, **4**, 7334.

Table of Contents

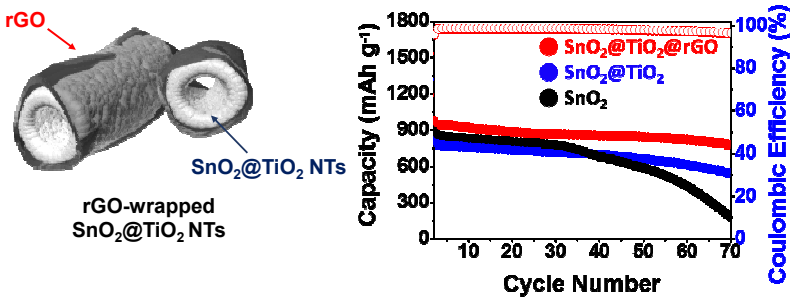

Reduced graphene oxide (rGO)-wrapped SnO_2@TiO_2 nanotubes (NTs) anodes exhibit superior rate capability and cycle retention due to formation of stable solid electrolyte interphase (SEI) layer achieved by TiO_2-coated layer and enhanced electrical conductivity through rGO.